Phase ordering and its effect on magnetic and structural properties of FeRh ultrathin films

Q. J. Yap, J. J. Qiu, P. Luo, J. F. Ying, G. C. Han, D. E. Laughlin, J.-G. Zhu, T. Kanbe, and T. Shige

Citation: Journal of Applied Physics **116**, 043902 (2014); doi: 10.1063/1.4890032
View online: http://dx.doi.org/10.1063/1.4890032
View Table of Contents: http://aip.scitation.org/toc/jap/116/4
Published by the American Institute of Physics

JOURNAL OF APPLIED PHYSICS **116**, 043902 (2014)

Phase ordering and its effect on magnetic and structural properties of FeRh ultrathin films

Q. J. Yap,[1] J. J. Qiu,[1] P. Luo,[1] J. F. Ying,[1] G. C. Han,[1] D. E. Laughlin,[2] J.-G. Zhu,[2] T. Kanbe,[3] and T. Shige[3]
[1]*Data Storage Institute, A*STAR (Agency for Science, Technology and Research), DSI Building, 5 Engineering Drive 1, Singapore 117608*
[2]*Data Storage Systems Center, Carnegie Mellon University, Pittsburgh, Pennsylvania 15213, USA*
[3]*Showa Denko K.K., 13-9, Shiba daimon 1-Chome, Minato-ku, Tokyo 105-8518, Japan*

(Received 31 March 2014; accepted 1 July 2014; published online 22 July 2014)

Applications using FeRh for controllable exchange coupling of two magnetic layers with in-plane and out-of-plane anisotropies require ultrathin (∼10 nm) films with pure antiferromagnetic (AF) FeRh α'' phase at room temperature (RT). However, it is also well known that the antiferromagnetic-ferromagnetic (AF-FM) transition of FeRh is sensitive to composition and deteriorates at low thicknesses. Hence, in this work, we study the composition-dependent phase ordering of co-sputtered FeRh thin films at ultrathin thicknesses of ∼10 nm. As the ultrathin films get richer in Rh, the appearance of α'' phase is typically characterized magnetically by a sudden drop in RT moment, and structurally by a slight decrease in degree of B2 chemical ordering with a sharp decrease in c-axis lattice constant. These observations are consistent with the FeRh phase diagram where FeRh abruptly enters the AF α'' phase once it becomes slightly disordered. Dependences of magnetic transition parameters on composition were also described. Moreover, higher sputtering powers possibly allow the formation of purer α'' phase with less γ-face centered cubic phase impurities. Consequently, a composition optimized 10 nm film shows a relatively low residual moment (13.5 emu/cc), thus suggesting good AF phase formation. In addition, correlation of the magnetic transition parameters with the crystal structural parameters reveal that the maximum rate of AF-FM transition ($R_{max,h}$) and the corresponding total change in magnetization (ΔM_h) interestingly shows linear dependence on the c-axis lattice constant, but would depart from this linearity under certain conditions, i.e., when grain sizes were large, crystallinity was improved and Fe content was high. © *2014 AIP Publishing LLC*. [http://dx.doi.org/10.1063/1.4890032]

I. INTRODUCTION

FeRh is known to exhibit antiferromagnetic (AF) to ferromagnetic (FM) transition upon heating to temperatures above room temperature (RT) and vice versa upon cooling to room temperature.[1] Due to this interesting property, it has attracted much interest especially for magnetic memory applications.[2–5] In this work, we look at inventions that use FeRh to lower the switching field of the storage layer (SL), which is typically a magnetic layer that stores information in the form of the magnetization direction of magnetic domains in hard disk media or in magnetic random access memory (MRAM).[2,3] For example, there have been reports on how FeRh could lower the anisotropy and coercivity of FePt in FeRh-FePt bilayer films.[6–8] Other works focus on tri-layers utilizing FeRh as an exchange coupling inter-layer.[2,3,9] This work attempts to develop FeRh suitable for such tri-layer structures, which comprises a thin FeRh layer inserted in between a magnetic assist layer (AL) with an anisotropy parallel to the film plane, i.e., in-plane magnetic anisotropy and a magnetic SL with strong anisotropy perpendicular to the film plane, i.e., perpendicular magnetic anisotropy (PMA). This structure is also termed as the binary anisotropy media (BAM) structure.[2] When the FeRh interlayer is in the AF phase, AL and SL are in the decoupled state. When FeRh is heated into the FM phase, it couples the AL and SL, thus reducing the PMA of the SL and the required switching field.

For BAM to work, two important properties of the FeRh layer are required. First, unlike in bilayer structures where FeRh can be up to 60 nm thick,[8] an ultrathin thickness (<10 nm) is preferred for the tri-layered BAM. In the FM phase, the FeRh which is sandwiched in between the SL and the AL needs to be at an ultrathin thickness to allow the AL (in-plane) to couple strongly with the SL (perpendicular to plane) such that the exchange coupling strength is sufficient to reduce PMA of the SL for easy switching. In the AF phase, the FeRh should be below a critical thickness so that the inherent pinning strength at the AF/FM interface is so low that it will not influence the PMA and thermal stability of the SL. However, it is well known that the antiferromagnetic-ferromagnetic (AF-FM) transition deteriorates significantly at ultrathin thicknesses.[10,11] The reason for this is not yet well understood. Several mechanisms have been proposed to understand the formation of FM phases in the ultrathin FeRh films.[12–14] Second, another required property would be the purity of the AF α'' phase FeRh prepared. This is because any residual FM moment that exists in the form of impurities (e.g., FM α' phase, FM sites arising from defects) would induce unwanted AL-FeRh-SL coupling in the decoupled state at RT and thus influence the thermal stability of the SL. To achieve high purity, the composition should be carefully controlled with as small a distribution as possible because the α'' phase exists only in a very narrow region on the Rh-rich side of the FeRh phase diagram.[15] One practical way to tune composition is through the controlling of powers used for the co-sputtering of pure Fe and Rh targets.

To date, only a few works study the composition variation of FeRh thin films.[16–18] Most works also look into FeRh films deposited on glass or MgO(100) substrates which are not compatible with conventional semiconductor processes and MRAM. Moreover, most works also focus on films thicker than 80 nm, which are likely to have larger grains and different film morphology as compared to the ultrathin films. Hence, if there is morphology dependent composition distribution across the film, it might be necessary to study composition at an ultrathin thickness in order to obtain the best possible α'' phase which yield properties that fit application requirements.

It is noted that in order to support application potential, there is an acute need to demonstrate the reduction of PMA of the storage layers, by depositing and characterizing relevant structures, such as the BAM structure. However, before this can be done, we have decided to focus our efforts on tackling the more fundamental problem of removing the RT residual moment of FeRh at low thicknesses, as any residual moment can significantly deteriorate the functionality of the BAM structure as explained above.

Thus, in this work, the focus is on the ultrathin (∼10 nm) aspect of FeRh and its properties with respect to its composition, with an aim to obtain minimal residual moment by obtaining the purest possible AF α'' phase through careful composition optimization. As a result, we investigate the composition variation of co-sputtered FeRh films deposited on MgO buffer layers grown on thermally oxidized Si(100) substrates, particularly at an ultrathin thickness of 10 nm.

II. EXPERIMENT

FeRh films were deposited on thermally oxidized Si(100) wafers with 5 nm MgO buffer layers by co-sputtering of pure Fe and Rh targets in an ultrahigh vacuum chamber with an ultimate pressure of <2E-6 Pa. Film thicknesses were controlled by time calibrated from known deposition rates of films deposited at room temperature. Compositions of the films were varied by controlling the sputtering power of each target. Ar working gas with a purity of 99.999% was used.

This work covers 3 series of samples for which composition is varied. We have decided to study FeRh at bulk thicknesses (80 nm) first since the characterization and data interpretation of FeRh are more difficult at 10 nm. In the first series of samples, film thicknesses were kept at 80 nm. Rh target power (P_{Rh}) was fixed at ∼90 W and Fe target power (P_{Fe}) was varied from 110 W to 150 W at 5 W intervals (the smallest scale division in the target power meter) with 130 W and 135 W omitted. Substrate temperature (T_s) was 400 °C and working gas pressure was 0.105 Pa. After depositing this 80 nm sample set, we deposit different series of 80 nm samples with varying T_s and pressure (not reported here) and find that the optimized T_s is 650 °C (results not published) and the optimized pressure is 0.059 Pa.[19]

At the optimized T_s (650 °C) and pressure (0.059 Pa), we proceeded to deposit the second and third series of samples, which consist of FeRh films which are 10 nm thick. For the second series of samples (termed as "Set A"), P_{Fe} was fixed at 80 W and P_{Rh} was varied from 87.5 W to 97.5 W at 2.5 W intervals (half the smallest division in the target power meter). For the third series of sample (termed as "Set B"), P_{Rh} was fixed at 200 W while P_{Fe} was varied from 175 W to 155 W at 5 W intervals. Thus, the overall sputtering powers used for Set A were lower than that used in Set B. It is noted here that the T_s and pressure used for Set A and Set B is different from the 80 nm sample set. Hence, we emphasize here that the main focus of the work is on the 10 nm sample sets. Thus, only general comparisons can be made between the 80 nm sample set and the 10 nm sample sets.

Subsequently, these films were characterized for their magnetic properties using a superconducting quantum interference device (SQUID) magnetometer. For SQUID magnetometer measurements, all samples were first cooled to 100 K under a zero magnetic field. Then, they were heated up to 400 K under a magnetic field like 1 kOe or 50 kOe, during which a magnetization (M) vs temperature (T) heating measurement was obtained. Subsequently, they were cooled without changing the field during which another M-T cooling measurement was obtained. Furthermore, the composition of selected films within each sample set was estimated using X-Ray Photoelectron Spectroscopy (XPS) depth profiling. Structurally, the samples were characterized using x-ray diffraction (XRD) in the Bragg-Brentano geometry. For the scans with 2θ ranging from 25° to 75°, Ni 0.02 mm filter was used to reduce the intensity the Cu kβ radiation from the Si(400) diffraction peak as it overlaps with the FeRh(002) peak. For the 10 nm sample sets, we used Ni 0.04 mm filter to further reduce the kβ peak and performed additional separate scans of a few degrees at 2θ angles near the FeRh(001) and FeRh(002) peak with long scan times for better signal to noise ratio. Peak parameters were then extracted using "Highscore Plus" software provided with the XRD tool. Rocking curves were also performed at the FeRh(001) peak. The morphology of the ultrathin films was examined using atomic force microscopy (AFM). Grains in each image were marked at 50% of the maximum height and analyzed for their sizes using the open source software "Gwyddion."

III. RESULTS AND DISCUSSION

For each series of samples, the films are described magnetically and structurally such that the film properties are looked at in a direction towards Rh-richer compositions. The focus of this work is on the 10 nm sample sets but we first look at the 80 nm sample set to have a general idea of composition dependence of bulk films. Figs. 1(a)–1(c) show the typical XRD profiles of the 80 nm sample set. All samples show that only B2 phase [as identified by α-FeRh(001) and α-FeRh(002) peaks] is present, except for the last sample in the series which has the richest Rh-content [smallest P_{Fe} (110 W)] that shows both B2 phase and γ-face centered cubic

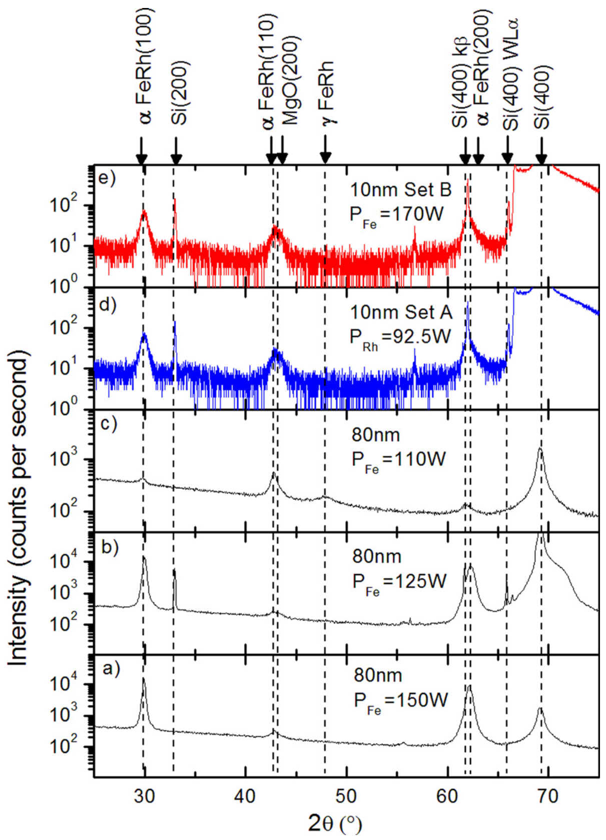

FIG. 1. Typical XRD profiles of 80 nm sample set (a)–(c), 10 nm sample Set A (d), 10 nm sample Set B (e).

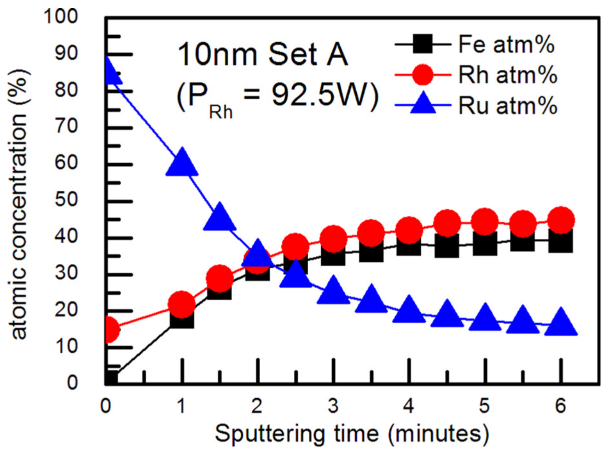

FIG. 2. Typical XPS depth profile of a 10 nm sample. From the flat region of the curve (5–6 min), Rh content is divided over the sum of Fe and Rh content to give actual Rh atm. %.

(FCC) phase. Table I shows the film composition estimated using XPS. The composition of each sample is expressed in terms of Rh atm. % which is given by the percentage of Rh content over the sum total of the Fe and Rh content determined from the flat region of each XPS depth profile. A typical XPS depth profile is shown in Fig. 2. From Table I, the films in the 80 nm film set ranges from 50.1 to 56.2 Rh atm. %. The Rh-richest sample (56.2 Rh atm. %) falls within a region in the phase diagram[15] that is expected to exhibit both B2 and FCC phases. This observation is thus consistent with the XRD data described above.

Furthermore, peak parameters like the out of plane lattice constant (c), the full width at half maximum (FWHM) of the FeRh(001) rocking curve, and the square root of the ratio of the integrated intensity of the FeRh(001) superlattice peak to that of the FeRh(002) fundamental peak $[(I_{001}/I_{002})^{1/2}]$ were extracted from the XRD profiles and plotted in Fig. 3. The closed squares show the parameters for the 80 nm sample set.

For the first series of 80 nm samples, when the films get Rh-rich, specifically when Fe target power reduces by a mere 5 W from 130 W to 125 W, there is an abrupt drop in room temperature moment in the film (not shown here). As shown by closed squares in Fig. 3(a), this is accompanied by a slight drop in $[(I_{001}/I_{002})^{1/2}]$, which indicates that the degree of chemical ordering of the FeRh B2 structure has

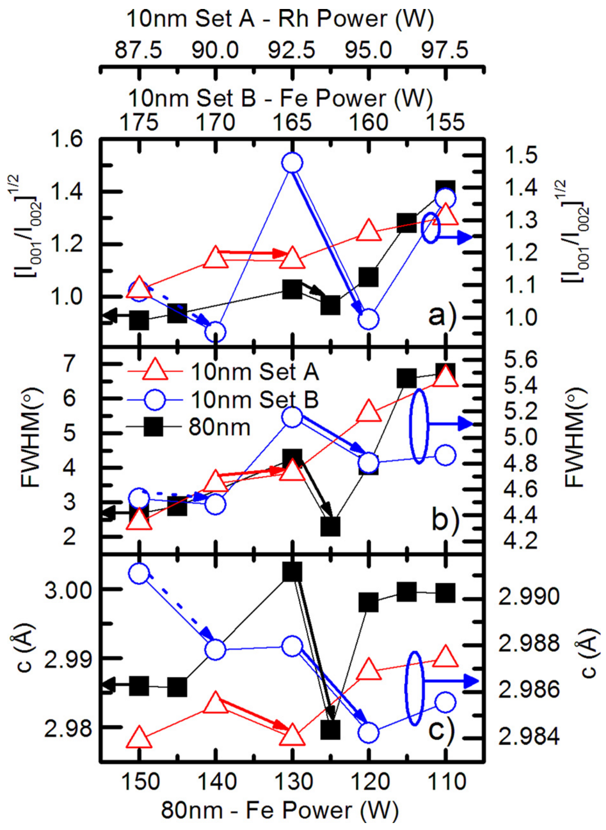

FIG. 3. Parameters extracted from XRD profiles for the 80 nm sample set and 10 nm sample sets.

TABLE I. Estimated film composition from XPS depth profiles.

Sample set	P_{Fe} (W)	P_{Rh} (W)	Pressure (Pa)	Rh atm. % [a]
80 nm	150	~90	0.105	50.1
80 nm	125	~90	0.105	53.6
80 nm	110	~90	0.105	56.2
10 nm Set A	80	92.5	0.059	53.2
10 nm Set A	80	97.5	0.059	55.9
10 nm Set B	170	200	0.059	51.6
10 nm Set B	155	200	0.059	53.8

[a] Rh atm. % is given by the percentage of Rh content over the summed Fe and Rh content from the flat region of the XPS depth profile as shown in Fig. 2.

decreased a little. These observations are consistent with the FeRh phase diagram.[15] First, the phase diagram shows that a small increase of Rh atomic percentage (atm. %) by <2.5 atm. % causes FeRh to enter the AF α'' phase from the FM α' phase. Thus, room temperature moment is expected to drop significantly and abruptly as described. Second, since the α'' phase is slightly off equiatomic on the Rh-rich side of the phase diagram, it is also expected to be slightly disordered chemically, assuming perfect order is achieved when FeRh is equiatomic. Hence, the observed decrease in $[(I_{001}/I_{002})^{1/2}]$ is reasonable.

Closed squares in Fig. 3(b) show the FWHM of the FeRh (001) rocking curve as a function of Fe content expressed in terms of P_{Fe}. Besides $[(I_{001}/I_{002})^{1/2}]$ decreasing when P_{Fe} decreases from 130 W to 125 W, FWHM also decreases abruptly. Thus, this implies that a sharp improvement in crystalline quality accompanies the appearance of the α'' phase as Rh content increases beyond a certain point. Furthermore, the c lattice constant also decreases sharply, which is an indication of the formation of the α'' phase since it is well known that the AF α'' phase remarkably exhibits 1% less volume as compared to the FM α' phase without significant change in crystallographic structure.[20] Such behavior is also observed in other works.[18] As the films continued to get Rh-rich, $[(I_{001}/I_{002})^{1/2}]$, FWHM and c start to increase and the AF-FM transition correspondingly deteriorates, i.e., transition is broadened with less total change in magnetization (not shown here). Such deterioration is most likely due to the increased formation of Rh rich γ-FCC phase which was reported to hinder B2 ordering and cause transition to deteriorate.[17,21] However, it is noted that some FCC phase may already be present in the film before P_{Fe} decreases to 110 W but in small amounts such that it is not sufficient to be measured by XRD. Only when P_{Fe} reaches 110 W, then the γ-FCC peak appear in the XRD profile. Even then, the peak intensity is relatively weak as seen in Fig. 1, thus suggesting that this phase is disordered and not well-textured.

We now move on to 10 nm sample Set A which is deposited at a lower power range than Set B. XRD confirms that all films are predominantly B2 phase as no peaks showing FCC phase can be detected, as seen from the typical profile in Fig. 1(d). From Table I, film compositions were estimated to range between 50.3 and 55.9 Rh atm. % with an increase of ∼1.4 Rh atm. % per 2.5 W increase of P_{Rh} (assuming linearity). Fig. 4 shows M-T plots for 10 nm sample Set A. In particular, specific parameters describing the M-T transitions such as the total change in magnetization (ΔM) and the minimum and maximum magnetization (M_{min} and M_{max}) for both the heating and the cooling transitions (as denoted by subscripts h and c respectively) are extracted and plotted against Rh composition in terms of P_{Rh} in Fig. 5. Trends similar to that in the 80 nm sample set are clearly observed. From Fig. 5, when the film gets Rh-rich, specifically when P_{Rh} increases by just 2.5 W from 90 W to 92.5 W, an abrupt drop in low temperature residual moment (M_{min}) is observed, suggesting conversion of α' phase into α'' phase. This is again accompanied by a slight decrease in $[(I_{001}/I_{002})^{1/2}]$ and a significant decrease in c [open triangles in Figs. 3(a) and 3(c)], thus also suggesting the appearance of α'' phase. As the films continued to get Rh-rich, $[(I_{001}/I_{002})^{1/2}]$, c and FWHM again increase, while transition parameters deteriorated, i.e., ΔM decreases and M_{min} increases (Fig. 5). These results imply that the residual moment in these 10 nm samples is dominated by bulk properties instead of the surface or interface effect. Thus, the film with $P_{Rh} = 92.5$ W is considered the sample with the purest α'' phase in Set A.

In addition, Fig. 6 shows other parameters like the transition temperature ($T_{tr,h}$ and $T_{tr,c}$ for heating and cooling transitions, respectively), which is defined as the temperature

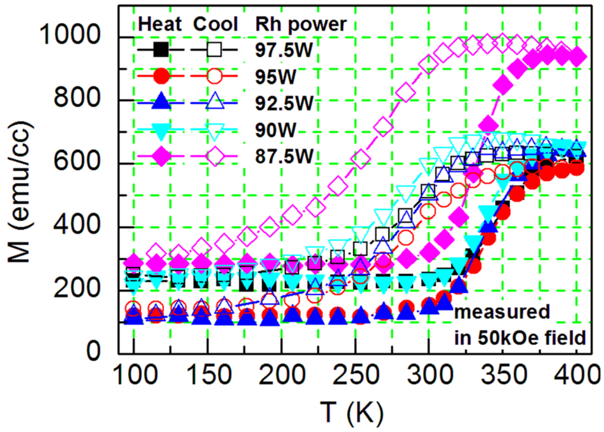

FIG. 4. M-T plots for 10 nm sample Set A.

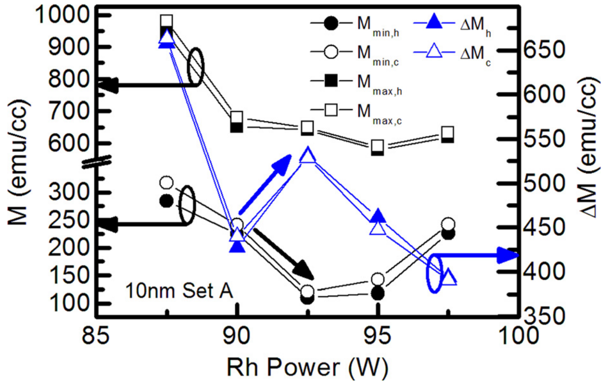

FIG. 5. Transition parameters M_{min}, M_{max}, and ΔM extracted from Figure 4 (10 nm sample Set A).

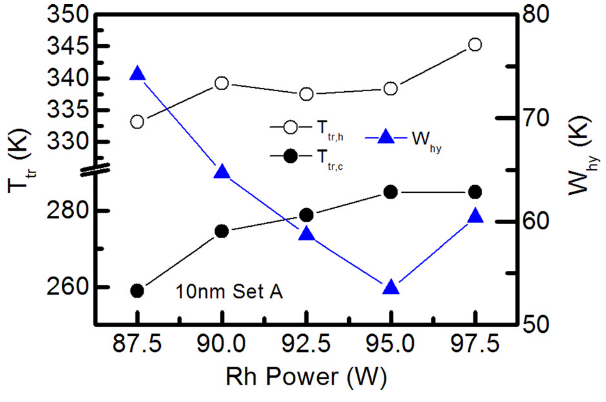

FIG. 6. Transition parameters T_{tr} and W_{hy} extracted from Figure 4 (10 nm sample Set A).

(T) at which the magnetization changed to half the total change in magnetization, i.e., $T_{tr} = T$ at $M_{min} + 1/2\Delta M$ (linear interpolation of M-T plot is performed using Origin software). As Rh content increases, $T_{tr,h}$ shows a local minimum of 337 K at $P_{Rh} = 92.5$ W, where α'' phase is the purest and a global minimum of 333 K at $P_{Rh} = 87.5$ W. Thus, it is inferred that $T_{tr,h}$ is controlled by 2 forces, i.e., the purity of the α'' AF phase and the amount of α'' FM phase impurities present. We suggest that the greater the amount of α'' AF phase present initially before the onset of AF-FM transition, the greater the overall driving force of the AF-FM transition that causes the transition to shift to lower temperatures, leading to a lower $T_{tr,h}$. Since the proportion of α'' phase is deduced to be maximum at $P_{Rh} = 92.5$ W, we expect $T_{tr,h}$ to be lowered at this composition (local minimum). However, α' FM phase impurities on the Fe-richer side can also act as FM nucleation sites which assists AF-FM transition and cause transition to shift to lower temperatures ($T_{tr,h}$ decrease) as well. Thus, on the Fe-richer side ($P_{Rh} = 87.5$ W), the effect of α' FM phase impurities could dominate such that it causes $T_{tr,h}$ to decrease significantly (global minimum).

As for the cooling (FM-AF) transition, it seems that $T_{tr,c}$ depend directly on the Rh content in the film, i.e., $T_{tr,c}$ increases and saturates as Rh content increases. Thus, the FM-AF nucleation mechanism seems to be quite different. It could be that the FM impurities on Fe-rich side serve as FM pinning sites throughout the transition, thus delaying the cooling transition and decreasing $T_{tr,c}$ when film composition is on the Fe-richer side. As a result, we see that the heating and cooling transition behavior behaves differently with respect to composition. The width of temperature hysteresis (W_{hy}), which is defined as $W_{hy} = T_{tr,h} - T_{tr,c}$, is thus the net effect of the heating and cooling transition behaviors, which is found to be narrowest when the film is slightly Rh-richer than the purest α'' composition.

The third series of 10 nm samples (Set B) were co-sputtered at target powers that are higher than that in the second series (Set A) to investigate the sputtering power dependence of the magnetic properties. XRD again confirms that no FCC phase can be detected for all the samples in the series and a typical profile is shown in Fig. 1(e). From Table I, XPS confirms that the composition falls in a range that is similar but narrower when compared with previous sample sets, i.e., 50.8% to 53.9 Rh atm. % with 0.77 Rh atm. % change per 5 W increase in P_{Fe} (assuming linearity).

Fig. 7 shows the M-T plots, from which M_{min}, M_{max}, and ΔM were extracted and shown in Fig. 8, while the open circles in Fig. 3 show structural parameters of the samples. With reference to the figures, as the film gets Rh rich, particularly when P_{Fe} reduces by just 5 W from 175 W to 170 W, a sharp drop in M_{min} and rise in ΔM to 677 emu/cc is again detected, and this was accompanied by a reduction in $[(I_{001}/I_{002})^{1/2}]$ and c. Again, the reduction in c most likely corresponds with the disappearance of α' phase (of higher lattice constant) and the appearance of a highly pure α'' phase.

As the films continued to get Rh-rich, although transition properties deteriorated (ΔM decreased and M_{min} increased), $[(I_{001}/I_{002})^{1/2}]$, FWHM and c did not rise steadily like in the second series of samples. Instead, a second drop in c was detected (Fig. 3(c)) and ΔM simultaneously dropped to about 500 emu/cc. This second drop in c could be attributed to strain induced lattice distortions due to higher sputtering power. In addition, since the films entered the Rh-richer regime, some Rh-rich paramagnetic γ-FCC phase or Rh-terminated grains might have appeared which might cause strain induce lattice distortions in the system which could originally be purely body centered cubic (BCC) (both α'' and α' phase are BCC) when in the Fe-richer regime. Additionally, in the Rh-rich regime, less Fe-rich FM nucleation sites are now available within the grains to help with the AF-FM transformation. Hence, the AF-FM transformation for the Rh-richer sample ($P_{Fe} = 160$ W) may experience greater difficulty as compared to that for the Fe-richer sample ($P_{Rh} = 170$ W), and thus might experience a less complete AFM-FM transformation, explaining the lower ΔM exhibited (~500 emu/cc). For example, some AF phase could have been retained at the grain center even after the AF-FM transformation as suggested in Ref. 22.

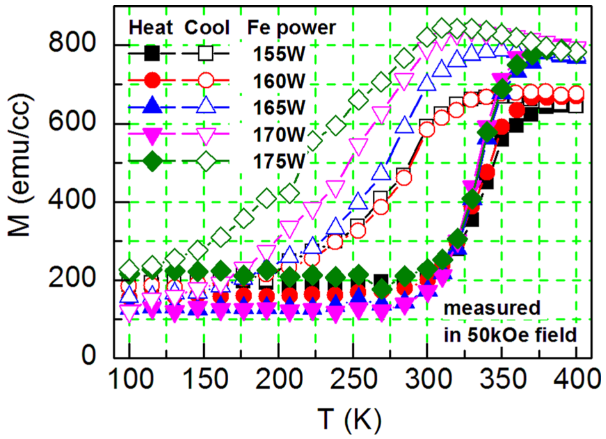

FIG. 7. M-T plots for 10 nm sample Set B.

Fig. 9 shows other extracted transition parameters like $T_{tr,h}$, $T_{tr,c}$, and W_{hy}. We can see that there is again a local minimum for $T_{tr,h}$ at the composition where α'' phase is deduced to be purest. Thus, similar reasoning employed earlier in Set A can be used to describe this behavior. However, on the Fe-richest side, no dip in $T_{tr,h}$ is observed. Thus, it could be that the Fe content has not increased sufficiently such that the effect of α' FM impurities is not yet observable.

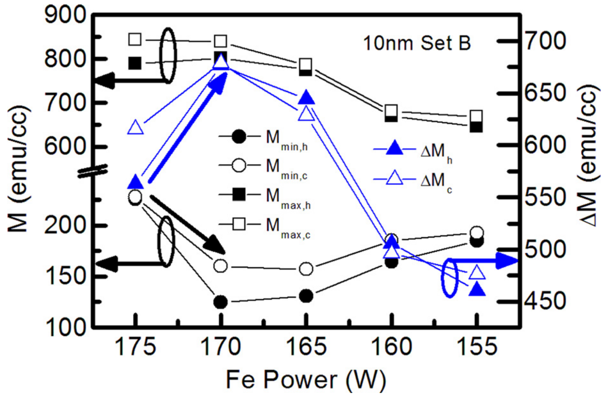

FIG. 8. Transition parameters M_{min}, M_{max}, and ΔM extracted from Figure 7 (10 nm sample Set B).

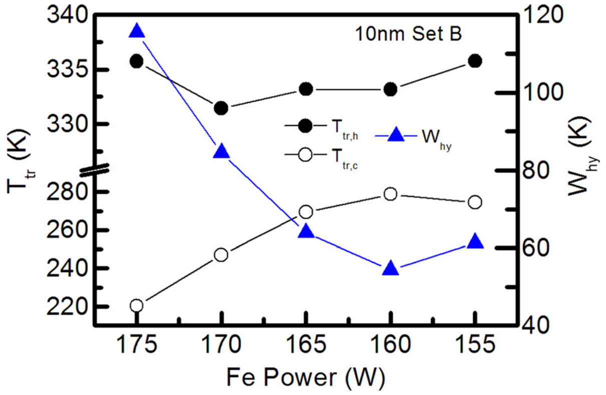

FIG. 9. Transition parameters T_{tr} and W_{hy} extracted from Figure 7 (10 nm sample Set B).

Moreover, $T_{tr,c}$ also has a trend similar to that in Set A, i.e., increases and saturates as Rh content increases. As a result, W_{hy} is again found to be narrowest at a composition that is slightly Rh-richer than the purest α'' phase.

Comparing the best performing (high ΔM with minimal M_{min}) sample from Set A and Set B, the one from Set B ($P_{Fe} = 170$ W, $\Delta M = 677$ emu/cc) exhibited a significantly higher ΔM than the one from Set A ($P_{Rh} = 92.5$ W, $\Delta M = 531$ emu/cc). Table I shows that the sample from Set B has film composition of 51.5 Rh atm. % while that from Set A has a film composition of 53.2 Rh atm. %. This means that the Set A sample is Rh-richer than the Set B sample, which could imply that the Set A sample has more paramagnetic Rh-rich γ-FCC phase impurities than the Set B sample, resulting in a lower ΔM. Thus, higher sputtering power seems to allow the formation of purer α'' phase with minimal γ-FCC phase impurities, while lower sputtering power causes unavoidable γ-FCC phase impurities even when composition is optimized. It is noted that these FCC impurities could appear in small amounts not detectable by XRD. As Rh adatoms are heavier, mobility is generally lower. Thus, lower sputtering power could cause a proportion of low energy Rh adatoms to cluster and form the undesirable FCC phases. In addition, the FWHM for the Set B sample is also narrower as compared to that for the Set A sample, suggesting better crystallinity is obtained with high power deposition. Thus, it is inferred that the formation of highly pure and crystalline α'' phase film with high ΔM (>550 emu/cc under 50 kOe field) and low M_{min} (<150 emu/cc under 50 kOe field) is only possible when higher target powers are used. In other words, high adatom mobility from high powered sputtering generates high crystallinity in the films and reduces the amount of γ-FCC phase impurities.

Fig. 10 shows the AFM images of the composition optimized films from the 80 nm sample set and the 10 nm sample sets (Set A and Set B). The root mean square (rms) roughness of the composition optimized 80 nm film is 3.03 nm, i.e., <5% of the actual film thickness (80 nm). Thus, we consider the 80 nm film to be continuous. For the 10 nm sample sets, the films have granular features with mean grain sizes of about 28 nm and 42 nm and roughness of about 2.66 nm and 3.14 nm for the composition optimized samples of Set A and Set B, respectively. Hence, it may be suggested that bulk films allow for easier nucleation of resultant magnetic phases since nucleation sites can easily propagate throughout the continuous bulk volume. Furthermore, more cooperative AF-FM transformation can occur across the volume due to coupling across FM nuclei during nucleation, thus explaining sharper AF-FM transitions as shown in Fig. 11. On the other hand, for 10 nm films, the small grain volume means nucleation activity is limited to a small volume and cooperative AF-FM phase transition is not promoted due to limited intergrain coupling, leading to broader transitions.

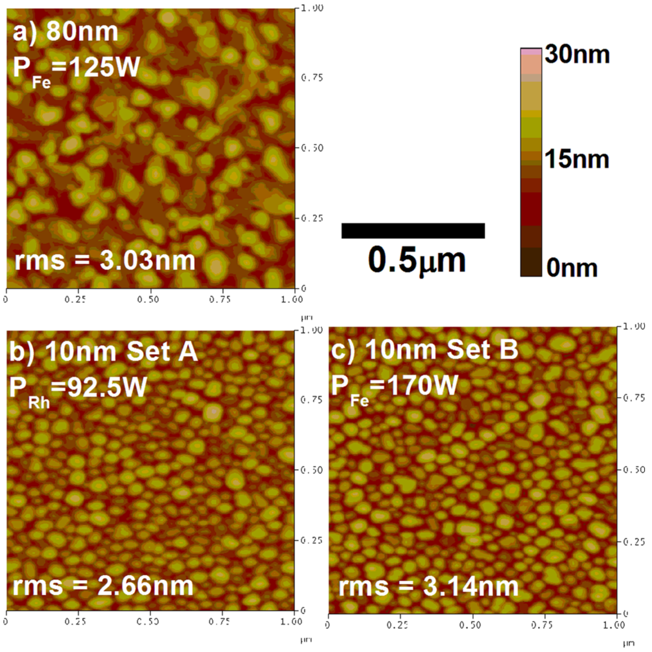

FIG. 10. AFM images comparing the morphology of the 80 nm sample set (a), the 10 nm sample Set A (b), and the 10 nm sample Set B (c).

Hence, despite the differences in sputtering conditions and film thickness, each of the three series of samples consistently show that the purest possible α'' phase can be obtained by tuning Rh content slowly. Typically, an abrupt increase in ΔM and decrease in M_{min}, as well as an abrupt decrease in both $[(I_{001}/I_{002})^{1/2}]$ and c are observed whenever

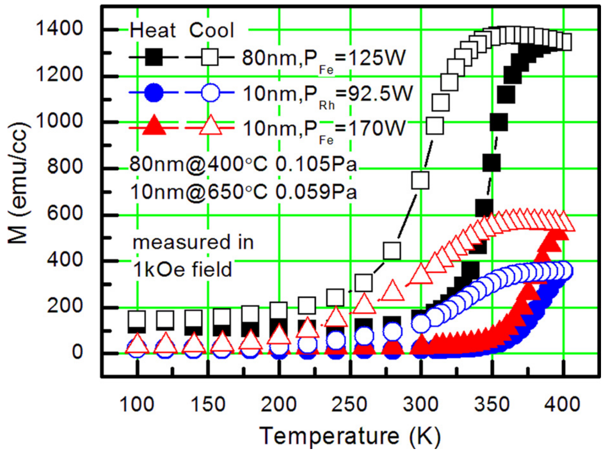

FIG. 11. M-T plots comparing the composition optimized samples from 80 nm sample set and the 10 nm sample sets.

α'' phase appears in the Rh-rich direction. Subsequently, the composition-optimized sample from the second series of samples (P_{Rh} 92.5 W) shows a low residual moment of 13.5 emu/cc under a field of 1 kOe (not shown here), which is significantly small as compared to the residual moment reported elsewhere.[10,11] When thickness is reduced to 3 nm using this sputtering condition, it is worthy to note that transition was still observable[23] when it is expected to almost disappear in some cases.[11] Moreover, α'' phase that are highly crystalline with high purity, low γ-FCC impurities, high ΔM and minimal M_{min} is most likely only possible when the adatoms have higher mobility. In addition, we have shown that residual moment is very sensitive to composition, such that a small change in ratio of target powers used during co-sputtering can reduce the residual moment significantly. We note that some residual moment still remains, which could essentially arise from other factors such as diffusion or surface or interfacial effects.[12,13,24–26]

Subsequently, for all the 10 nm films, the magnetic parameters such as ΔM and the maximum rate of transition during heating ($R_{max,h}$) are correlated with the structural parameters $[(I_{001}/I_{002})^{1/2}]$, FWHM and c. To clarify, the rate of transition (R) was determined by performing a first order differentiation on each of the M-T plots using Origin software, which computes the derivative at each point by taking the average of the slopes between the point and its two closest neighbors. Each measurement point was taken at 5 K intervals. Hence, there exists a maximum in each R-T plot for which the maximum value of the rate is labelled as $R_{max,h}$, where h denotes AF-FM transition. An interesting observation is shown in Figure 12. As c increases, both ΔM and $R_{max,h}$ decreased linearly (only $R_{max,h}$ shown), with the exception of 4 outlier points, for which both ΔM and $R_{max,h}$ were significantly higher. From the AFM images (not shown here), grain statistics also show that the samples corresponding to the 4 outlier points had mean grain sizes greater than 34 nm while those that fall within the linear region had mean grain sizes less than 34 nm. Furthermore, the FWHM (not shown here) of 3 of these 4 outlier points were found to be narrower compared to those in the linear region, which suggests that big grains could also mean better crystallinity. Moreover, the 4 outlier points also correspond to samples with relatively higher Fe content which implies that the samples could have more Fe-rich FM nucleation sites that aided the AF-FM transition, thus explaining the significantly higher $R_{max,h}$. Therefore, grain size, crystallinity, and Fe content most likely have a dominant effect on ΔM and $R_{max,h}$ while c has a secondary linear effect. The linear rise in $R_{max,h}$ as c shrinks could be attributed to differences in AF-FM nucleation growth dynamics that could arise from differences in proportion of α'' phase presence or film strain which causes a variation in c. On the other hand, ΔM and $R_{max,h}$ showed no particular dependence on ordering $[(I_{001}/I_{002})^{1/2}]$. Other magnetic transition parameters such as $T_{tr,h}$ and $T_{tr,c}$ and W_{hy} exhibited by the transition loops were also looked into but they showed no obvious correlation with $[(I_{001}/I_{002})^{1/2}]$, FWHM or c.

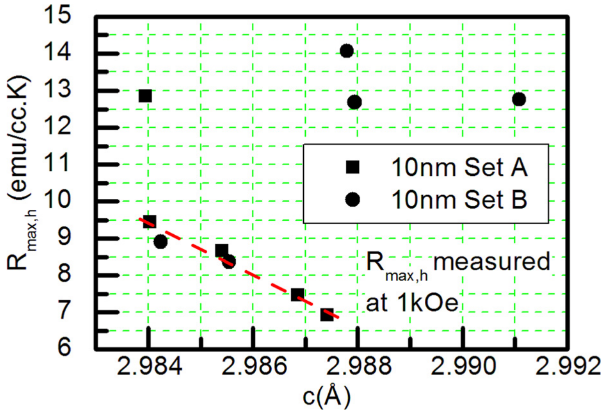

FIG. 12. $R_{max,h}$ of samples showing linear dependence with c and 4 outlier points that departs from this linearity when grain sizes were large, crystallinity were improved, and Fe content were high.

IV. CONCLUSION

Our results show that despite differences in sputtering conditions and film thickness used in the three series of samples, as Rh content increases in the film, an abrupt drop in M_{min} and an increase in ΔM, which implies an improvement of magnetic transition performances in the FeRh films, are found to be related to the reduction in lattice constant c, improvement of crystalline quality and slight chemical disorder. High sputtering power also tends to allow the formation of highly pure α'' phase with minimal γ-FCC phase impurities. A relatively low RT residual moment (13.5 emu/cc under 1 kOe field) is achieved for a composition optimized ultrathin 10 nm film. However, the residual moment is not yet removed completely and future work might be needed to reduce it to zero before the BAM structure can work. Eventually, to demonstrate the feasibility of BAM, future work should also include the deposition and characterization of BAM structures in order to demonstrate anisotropy reduction in storage layers. It is also noted that the grain sizes obtained at 10 nm are still quite large (~30 nm). Thus thickness and processing temperature have to be further reduced without rise in residual moment in order to give smaller grain sizes compatible with applications like heat assisted magnetic recording (HAMR). In addition, c play an important role in magnetic properties as linear dependences of ΔM_h and $R_{max,h}$ on c are found. However, when grain sizes are large, enhanced crystallinity and greater Fe content are also present and ΔM_h and $R_{max,h}$ could increase dramatically and depart from the mentioned linear dependence. This also emphasizes the importance of crystallinity as highlighted in another work in which good crystallinity could also suppress the low temperature FM moment of FeRh.[19] The results could be useful in providing insights for the realization of the use of FeRh in applications like recording media and MRAM.

ACKNOWLEDGMENTS

This work was supported by Showa Denko K. K., the Data Storage Systems Center at Carnegie Mellon University and Data Storage Institute, A*STAR (Agency for Science, Technology and Research).

[1] M. Fallot and R. Hocart, "Sur l'apparition du ferromagnétisme par élévation de température dans des alliages de fer et de rhodium," Rev. Sci. **77**, 498–500 (1939).

[2] J. G. Zhu and D. E. Laughlin, U.S. patent 8,211,557 (U.S. Patent and Trademark Office, Washington, DC, 2012).

[3] J. G. Zhu, Y. Luo, and X. Li, U.S. patent 7,826,258 (U.S. Patent and Trademark Office, Washington, DC, 2010).

[4] E. E. Fullerton, S. Maat, and J. U. Thiele, U.S. patent 7,372,116 (U.S. Patent and Trademark Office, Washington, DC, 2008).

[5] Y. Zhou, K. Takano, K. Liu, K. Zhang, L. Guan, M. Dovek, and J. Smyth, U.S. patent 8,004,794 (U.S. Patent and Trademark Office, 2011).

[6] J.-U. Thiele *et al.*, "Magnetic and structural properties of FePt-FeRh exchange spring films for thermally assisted magnetic recording media," IEEE Trans. Magn. **40**(4), 2537–2542 (2004).

[7] K. Y. Guslienko *et al.*, "Magnetization reversal via perpendicular exchange spring in FePt/FeRh bilayer films," Phys. Rev. B **70**(10), 104405-1–104405-6 (2004).

[8] J.-U. Thiele, S. Maat, and E. E. Fullerton, "FeRh/FePt exchange spring films for thermally assisted magnetic recording media," Appl. Phys. Lett. **82**(17), 2859 (2003).

[9] T. J. Zhou *et al.*, "The concept and fabrication of exchange switchable trilayer of FePt/FeRh/FeCo with reduced switching field," J. Appl. Phys. **111**(7), 07C116 (2012).

[10] I. Suzuki *et al.*, "Stability of ferromagnetic state of epitaxially grown ordered FeRh thin films," J. Appl. Phys. **105**(7), 07E501 (2009).

[11] D. Kande *et al.*, "Enhanced B2 ordering of FeRh thin films using B2 NiAl underlayers," IEEE Trans. Magn. **47**(10), 3296–3299 (2011).

[12] R. Fan *et al.*, "Ferromagnetism at the interfaces of antiferromagnetic FeRh epilayers," Phys. Rev. B **82**(18), 184418-1–184418-5 (2010).

[13] S. Lounis, M. Benakki, and C. Demangeat, "Ferromagnetic stabilization of ordered B2 FeRh thin films," Phys. Rev. B **67**(9), 094432-1–094432-5 (2003).

[14] Y. Kaneta *et al.*, "Theoretical calculations for magnetic property of ferh inter-metallic compound with site-exchange defects," Jpn. J. Appl. Phys., Part 1 **50**(10), 105803 (2011).

[15] T. B. Massalski *et al.*, *Binary Alloy Phase Diagrams* (ASM International, 1990).

[16] K. Cher, T. Zhou, and J. Chen, "Compositional effects on the structure and phase transition of epitaxial FeRh thin films," IEEE Trans. Magn. **47**(10), 4033–4036 (2011).

[17] Y. Ohtani and I. Hatakeyama, "Antiferro-ferromagnetic transition and microstructural properties in a sputter deposited FeRh thin film system," J. Appl. Phys. **74**(5), 3328 (1993).

[18] J. Van Driel *et al.*, "Compositional dependence of the giant magnetoresistance in Fe_xRh_{1-x} thin films," J. Appl. Phys. **85**(2), 1026–1036 (1999).

[19] G. Han *et al.*, "Suppression of low-temperature ferromagnetic phase in ultrathin FeRh films," J. Appl. Phys. **113**(12), 123909 (2013).

[20] M. Ibarra and P. Algarabel, "Giant volume magnetostriction in the FeRh alloy," Phys. Rev. B **50**(6), 4196 (1994).

[21] D. Kande, D. Laughlin, and J.-G. Zhu, "Origin of room temperature ferromagnetic moment in Rh-rich [Rh/Fe] multilayer thin films," J. Appl. Phys. **107**(9), 09E318 (2010).

[22] M. Loving *et al.*, "Structural evidence for stabilized ferromagnetism in epitaxial FeRh nanoislands," J. Phys. D: Appl. Phys. **46**(16), 162002 (2013).

[23] G. Han *et al.*, "Magnetic stability of ultrathin FeRh films," J. Appl. Phys. **113**(17), 17C107 (2013).

[24] Y. Ding *et al.*, "Bulk and near-surface magnetic properties of FeRh thin films," J. Appl. Phys. **103**(7), 07B515 (2008).

[25] J. W. Kim *et al.*, "Surface influenced magnetostructural transition in FeRh films," Appl. Phys. Lett. **95**(22), 222515 (2009).

[26] C. Baldasseroni *et al.*, "Effect of capping material on interfacial ferromagnetism in FeRh thin films," J. Appl. Phys. **115**(4), 043919 (2014).